E50 status report

S. Ajimura, T. Nakano, H. Noumi (Spokesperson),
K. Shirotori, Y. Sugaya, T. N. Takahashi, T. Yamaga
Research Center for Nuclear Physics (RCNP), Osaka University, Osaka 567-0047, Japan
K. Aoki, Y. Morino, K. Ozawa
Institute of Particle and Nuclear Studies (IPNS), High Energy
Accelerator Research Organization (KEK), Tsukuba 305-0801, Japan
T. Ishikawa
Research Center for Electron Photon Science
(ELPH), Tohoku University, Miyagi 982-0826, Japan
K. Tanida
Department of Physics and Astronomy, Seoul National University, Seoul 151-747, Korea
Y. Miyachi
Physics Department, Yamagata University, Yamagata 990-8560, Japan
M. Naruki
Department of Physics, Kyoto University, Kyoto 606-8502, Japan
Y .Ma, F. Sakuma
RIKEN, Saitama 351-0198, Japan
K. Miwa
Physics Department, Tohoku University, Miyagi 980-8578, Japan
T. Sawada, W. C. Chang
Institute of Physics, Academia Sinica, Taipei 11529, Taiwan
R. Honda
Department of Physics, Osaka University, Osaka 560-0043, Japan
J. K. Ahn
Physics Department, Korea University, Seoul 136-713 Korea
J. T. Goetz
Thomas Jefferson National Accelerator Laboratory, Newport News, Virginia 23606, USA
(Dated: July 8, 2015)

I. INTRODUCTION

E50 has been approved as the stage-1 status at the 18th PAC. The PAC noted as follows.

i) The collaboration should not underestimate the difficulties posed by the detection of the tiny charmed-baryon signal via the missing-mass technique, which should remain the main goal of the experiment.

ii) The PAC emphasizes the importance of collaborative work with lattice QCD theorists to establish a coherent picture of excited hadrons with charm and strange quarks.

Keeping in mind these notes, we continuously keep close discussions with theorists and proceed preparation works on development of key detectors for the E50 experimental setup.

Recent progress for the theoretical estimations of the $\pi^- p \to \Lambda_c^+ D^{*-}$ reaction is briefly reported in section I A. Although it is still not easy to establish excited hadrons in Lattice QCD calculations, we follow a recent progress of the Lattice studies.

The above-mentioned theoretical estimation suggests that a production cross section of the $\pi^- p \to \Lambda_c^+ D^{*-}$ reaction is at a level of a few nb at a beam momentum of 20 GeV/c, as mentioned in section I A. In designing the detector system, we assume a typical production cross section of 1 nb in the $\pi^- p \to \Lambda_c^+ D^{*-}$ reaction. We have shown a sensitivity at a level of 0.1 nb in the proposal. However, we recognize key issues to develop a Ring-Image Čerenkov (RICH) counter for K/π identification in a range of 2$\sim$16 GeV/c, high-rate trackers, and High-speed data acquisition (DAQ) system in order to achieve the design performance. Below in this document, the statuses of the preparation of the experimental apparatuses, the RICH counter, the high-rate tracking detectors, the choice of detectors for charmed baryon spectrometer and the DAQ system are described.

A. Collaborations to theorists

We have refined the estimation of the cross section of the $\pi^- p \to \Lambda_c^+ D^{*-}$ reaction, based on two different theoretical frameworks, the reggeon exchange model and the effective Lagrangian method [1]. We refer to measured cross section data in the $\pi^- p \to \Lambda K^{*0}$ reaction. We have found in total that the reggeon exchange model excellently reproduces not only the energy dependence of the total cross section but also the differential cross sections as a function of t in the $\pi^- p \to \Lambda K^{*0}$ reaction, as shown in Figs. 1. The effective Lagrangian method substantially overestimates the cross section in the higher energy region. Assuming that the coupling constants of charmed meson and baryon vertices are the same as those for the strangeness production, we find that the total cross section for the charm production is about $10^3 \sim 10^6$ times smaller than the strangeness production depending on energy (s). Normalizing to the measured strangeness production cross section, we estimate

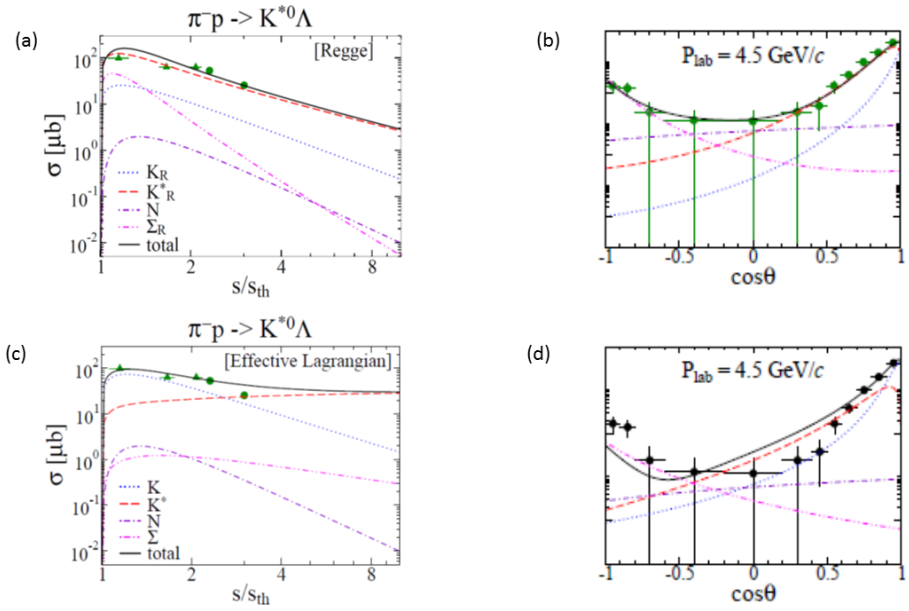

FIG. 1: Calculated total and differential cross sections of the $\pi^- \, p \to \Lambda \, K^{*0}$ reaction; (a) and (b) are total and differential cross sections calculated in the framework of the reggeon exchange model. (c) and (d) are those in the effective Lagrangian method. Here, s_{th} is the square of the threshold energy of the reaction.

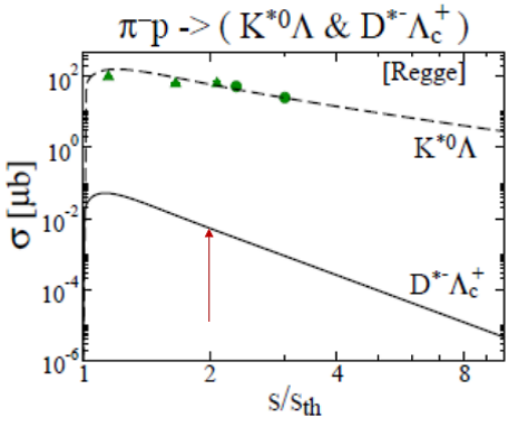

FIG. 2: Total cross sections of the $\pi^- \, p \to \Lambda_c \, D^{*-}$ reaction calculated in the framework of the reggeon exchange model. The quantity s/s_{th} is about 2 for the pion incident momentum of 20 GeV/c in the charm production, as indicated by an arrow.

that the charm production cross section is of order a few nb at a beam momentum of 20 GeV/c (Fig. 2), as consistent with the result of Ref. [2].

It is worthy to remark that there has been recently a progress on the hadron spectroscopy in Lattice QCD. By employing different types of interpolating fields for given quantum

numbers, it is demonstrated that the calculated light flavor baryons are rather well classified by $SU(6) \times O(3)$ as predicted by the constituent quark model [3]. This suggests that low lying modes are well described by constituent quarks as effective degrees of freedom. This encourages further to explore the dynamics of a colored light quark pair though heavy baryon spectroscopy. We expect that the distinction of collective and relative motions of the diquark pair (the λ and ρ modes) is particularly useful.

II. OVERVIEW OF EXPERIMENT

A. Experiment

The purposes of experiment are to observe and investigate the excited states of the charmed baryons [4]. The goal is to reveal the diquark correlation which is expected to be an essential degree of freedom to describe hadrons. The excitation energy and width are measured by the missing mass spectroscopy method by which all the excited states can be observed independent of the final state. The measurement of the production rate which strongly related to the spin/isospin configuration of charmed baryons can provide the unique information of the diquark correlation. In addition, the analysis of the decay particles and its decay chain which decays to the known states, the absolute decay branching ratio and the spin/parity of the excited states could also be determined. The systematic measurement of the excitation energy, the production cross section and the decay properties of the charmed baryon states can be performed.

1. High-momentum beam line

The experiment will be performed at the high-momentum beam line which is being constructed in the J-PARC hadron experimental facility [5]. The high-momentum beam line as shown in Fig. 3 will be upgraded to unseparated secondary beams with the high-intensity of more than 10^7 /spill and the momentum of up to 20 GeV/c. The momentum resolution of the secondary beams is expected to be less than 0.1% by using the momentum dispersive optical method. The high-momentum secondary beams with both high-intensity and high-resolution can be delivered to the experimental area. For measuring the beam momentum, a high-rate tracking device will be installed to the dispersive focal plane located at the entrance of the hadron hall. The scintillating fiber tracker is used for momentum measurement. The profiles of the delivered beam to the experimental target is also measured by the high-rate tracking device such as the scintillating fiber tracker. The fine segmented plastic scintillation counter to determine the reference timing and the Ring-Image Čerenkov counter for the identification of the beam particles are also installed at the upstream of the experimental target.

2. Spectrometer

For the charmed baryon production, the $\pi^-\ p \to Y_c^{*+}\ D^{*-}$ reaction is used with the beam momentum of 20 GeV/c. The D^{*-} meson decays by the $D^{*-} \to \bar{D}^0\ \pi^-$ channel (branching ratio of 67.7%). Then, the $\bar{D}^0$ meson decays by the $\bar{D}^0 \to K^+\ \pi^-$ channel (branching ratio of 3.88%). The decay products of K^+ and π^- of 2−16 GeV/c from $\bar{D}^0$ and

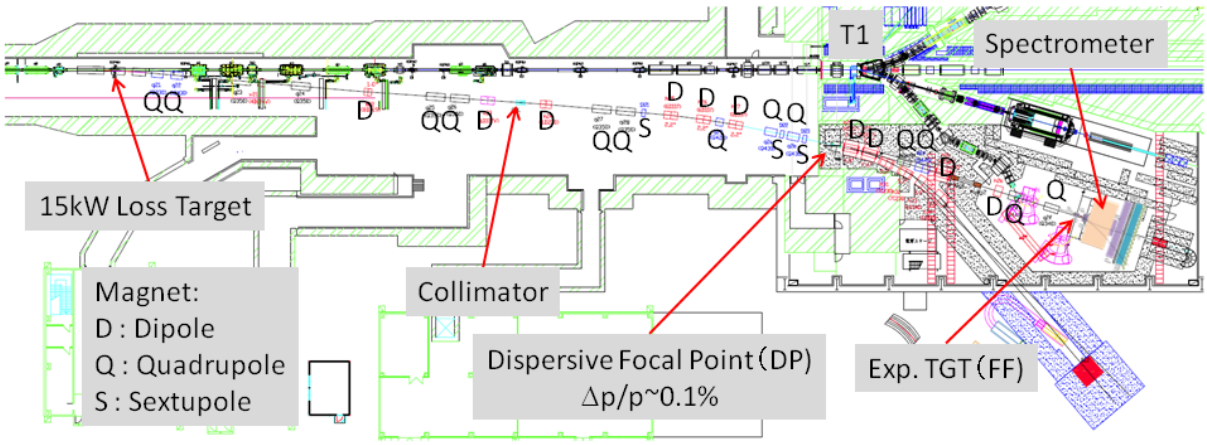

FIG. 3: The schematic view of the high-momentum beam line.

π^- of 0.5−1.7 GeV/c from D^{*-} are detected by the spectrometer. In addition, the decay measurement can be performed by detecting decay products from the produced Y_c^{*+}, such as as the $Y_c^{*+} \to \Sigma_c^{*++,0}\ \pi^{-,+}$, $Y_c^{*+} \to \Lambda_c^+\ \pi^+\ \pi^-$ and $Y_c^{*+} \to p\ D^0$ channels. The recoil momentum of Y_c^{*+} is measured by the missing mass method so that the mass of the decay products ($\Sigma_c^{*++,0}$ and D^0) can be obtained as a missing mass by only detecting the emitted pions and protons with the momentum of 0.2−1.5 GeV/c.

Figure 4 shows a conceptual design of the charmed baryon spectrometer [7]. In the case of the fixed target experiment with the high-momentum beam, all the generated particles, not only the scattered high-momentum particles from the D^{*-} decay but also the decay products from the produced Y_c^{*+}, are scattered to the forward direction. Therefore, the dipole magnet system which commonly measures both the particles from the D^{*-} decay for the missing mass method and the decay products from the produced Y_c^{*+} for the decay measurement is used for the charmed baryon spectrometer. For the spectrometer magnet, the FM cyclotron magnet which is used by the J-PARC E16 experiment [6] will be used.

Since the production cross section of charmed baryons is estimated to be 10^{-4} smaller than that of the strangeness production (10−100 μb of the $\pi^-\ p \to Y^*\ K^*$ reaction) [2], the charmed baryon production cross section of 1 nb was assumed for the experimental design. To obtain the production yield, the beam intensity of 6×10^7 /pulse is used. The high-rate detectors such as scintillating fiber trackers will be installed for the measurements of the beam momentum and profiles at focal plane and at the upstream of the experimental target, respectively. For beam particle identification, the high-rate Ring-Image Čerenkov counter will be used. The D^{*-} meson is measured by the forward detector system, the scintillating fiber trackers at the downstream of the target, and the drift chambers and the Ring-Image Čerenkov counter for detecting the high-momentum K^+ and π^- from $\bar{D}^0$ at the exit of the magnet. For measuring the slow π^- from D^{*-} at the forward region and the decay particles

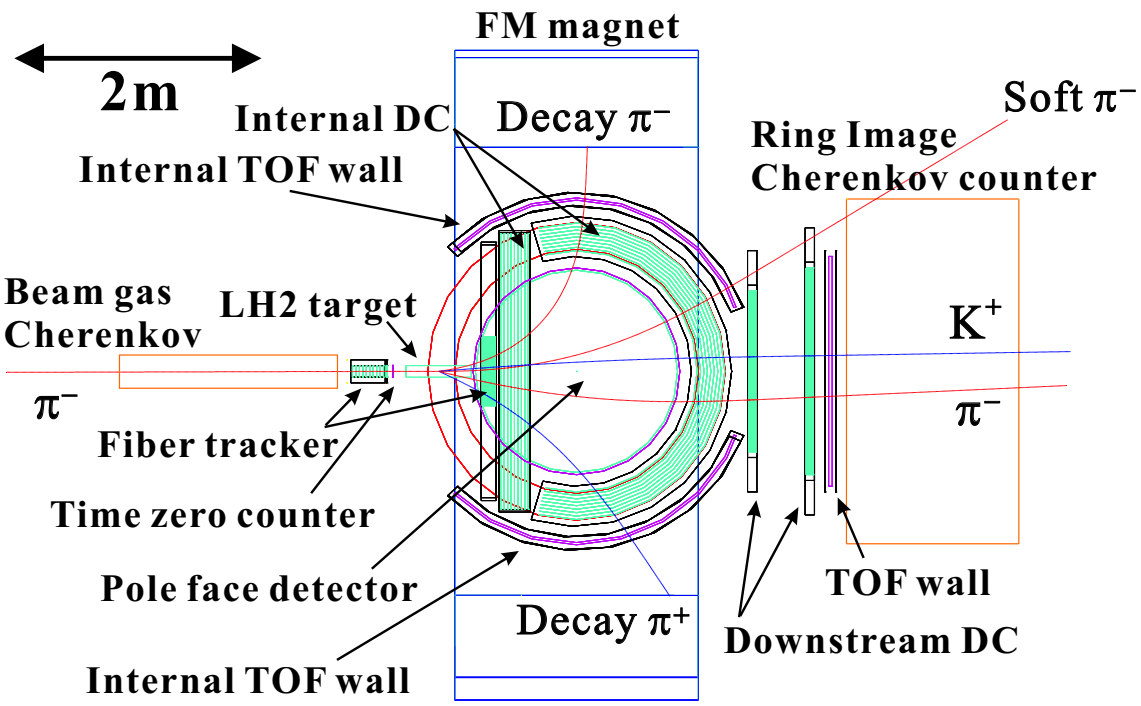

FIG. 4: The schematic view of the charmed baryon spectrometer.

from Y_c^* with the wide angular coverage, it is necessary to detect the particles inside of the magnet. The tracking detectors which have the large angular acceptance are installed at the downstream of the target. The horizontal and vertical directions can be covered by using the detectors installed around the magnet pole and the pad-type detector on the magnet pole face are installed, respectively.

3. Detectors

Table I shows the summary of the detectors for both beam measurement and the conceptual design of spectrometer.

B. Simulation

1. Basic performances of the spectrometer

The acceptance for detecting the D^{*-} decay was estimated to be 50−60% for the excitation states up to 1 GeV by assuming the angular distribution from the dominance of the t-channel production process. The momentum resolution of 0.2% was obtained at 5 GeV/c so that the invariant mass resolution for reconstructing the $\bar{D}^0$ and D^{*-} are estimated to be 5.5 MeV and 0.6 MeV, respectively. The missing mass resolution of excited states above

TABLE I: Summary of detectors.

Detector	Type	Size [mm×mm]	Resol. (σ)
Focal plane Fiber Tracker (FFT)	Plastic Scintillator	100×100	0.2 mm
Beam RICH (BRICH)	Gas Čerenkov		
Beam Fiber Tracker (BFT)	Plastic Scintillator	100×100	0.2 mm
Time definition counter (T0)	Plastic Scintillator	100×100	70 ps
Scat. Particle Fiber Tracker (SFT)	Plastic Scintillator	600×800	0.2 mm
Entrance Drift Chamber (DC1)	Planer Drift chamber	2400×800	0.2 mm
Exit Drift Chamber (DC2)	Cylindrical Drift chamber	3850×1200	0.2 mm
Downstream Drift Chamber (DC3)	Planer Drift chamber	1400×1200	0.2 mm
Downstream Drift Chamber (DC4)	Planer Drift chamber	1800×1600	0.2 mm
Downstream TOF (TOF)	Plastic Scintillator	2000×1800	100 ps
Scat. particle RICH (SRICH)	Gas and Aerogel Čerenkov		
Internal TOF (ITOF)	Resistive Plate Chamber	2600×1400	70 ps
Pole face TOF (PTOF)	Resistive Plate Chamber	1800×1800	70 ps

2.8 GeV/c^2 are estimated to be ∼10 MeV. For the decay measurement, both the polar and azimuthal angles are completely covered more than $\cos\theta_{CM} = -0.9 \sim -0.5$ for the $\Lambda_c(2940)^+ \to \Sigma_c(2455)^{++,0}\,\pi^{-,+}$ decay modes.

2. Expected missing mass spectrum

The background simulators of JAM [8] and PYTHIA [9] were checked by old experimental data in similar kinematical conditions. There are little available experimental data which clearly include the experimental information. For the invariant mass information by using the $\pi^-\,p$ reaction, the BNL experiment [10] with the beam momentum of 13 GeV/c and the CERN experiment [11] with that of 19 GeV/c can be available. The absolute value of the background around the $\bar{D}^{*-}$ mass region (±20 MeV) can be checked by the BNL data. In addition, there are the cross section data of the charged track multiplicity [12, 13]. It was found that both simulators have an ambiguity within only a factor from the experimental data. In particular, the JAM code well reproduced both background shapes and the absolute value, while the PYTHIA code reproduced with a difference of a few factor. The ambiguity of the absolute value around the $\bar{D}^*$ mass region (±20 MeV) was found to be 20−30%. For both simulator, the Lund string model was used for the hadronization process of which the parameterization of the input resonances were essential to reproduce the background shape. On the other hand, it was found that the contribution of the hard processes can be

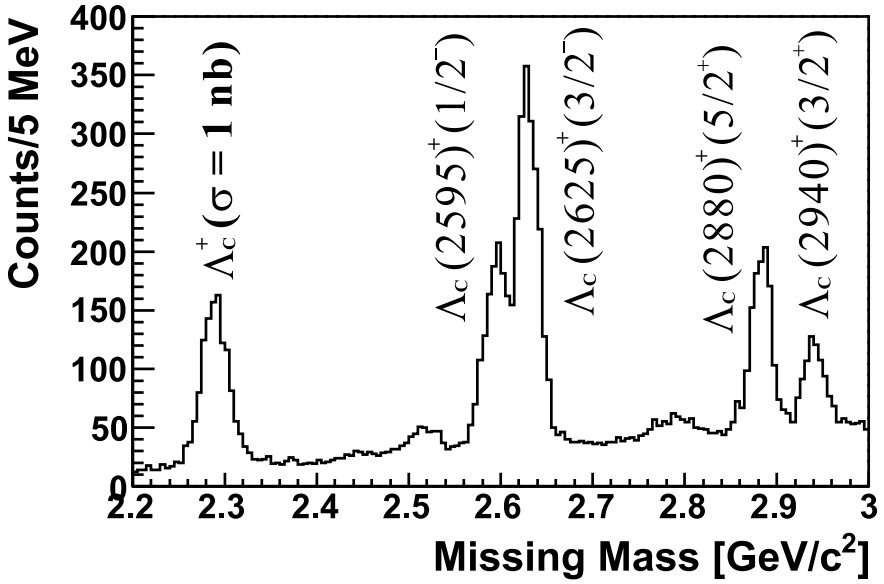

FIG. 5: The expected missing mass spectra simulated with the known charmed baryon states. The production rate from the theoretical calculation [2] in the case of $\sigma(\Lambda_c^+)$ =1 nb are used for the simulation. The λ-mode doublet states, such as $\Lambda_c(2595)(\frac{1}{2}^-)$ and $\Lambda_c(2625)(\frac{3}{2}^-)$ and excited states with $\Lambda_c(2880)(\frac{5}{2}^+)$ and $\Lambda_c(2940)(\frac{3}{2}^+)$ are enhanced. The spin/parity of $\Lambda_c(2940)$ has not been determined yet. In this simulation, it is assumed to be $J^P = 3/2^+$.

neglected.

The three kinds of the background processes, multi-meson production including the strangeness production, wrong particle identification and associated charm production, were studied. The strangeness production background is the main contribution of the background. By using the D^* tagging, the reduction of background events was found to be 2×10^6. Although the background level is still high by only using the D^* tagging, the other background reduction methods are applied for the farther background reduction. One method is the scattering angle selection of the K^+ and π^- which reconstruct the $\bar{D}^0$ mass in the center-of-mass system. The other is the event selections by using the kinematical conditions from the t-channel dominance of the $\pi^- + p \to Y_c^{*+} + \bar{D}^{*-}$ reaction. By taking into the reduction by the D^* tagging and the event selections, the average background level can be reduced to be 5 counts/MeV in the missing mass region of $2.2-3.4$ GeV/c^2. The background from the wrong particle identification by considering the performance of the PID detector was checked. The contribution of the missing mass spectrum was the same level as of the strangeness production. The associated charm production events were simulated by the EvtGen code [14]. The contribution was minor compared with the strangeness production and the wrong particle identification events. Finally, the the average background level was 11 counts/MeV in the

TABLE II: The relative production rates calculated by Ref. [2]. The production rates are normalized by the cross section of the ground state, $\Lambda_c^+(2286)$.

J^P	$\Lambda_c(\frac{1}{2}^+)$	$\Sigma_c(\frac{1}{2}^+)$	$\Sigma_c(\frac{3}{2}^+)$	$\Lambda_c(\frac{1}{2}^-)$	$\Lambda_c(\frac{3}{2}^-)$	$\Sigma_c(\frac{3}{2}^-)$	$\Lambda_c(\frac{5}{2}^+)$	$\Lambda_c(\frac{3}{2}^+)$
Mass [MeV/c^2]	2286	2455	2520	2595	2625	2820	2880	2940
Relative production rate	1	0.03	0.17	0.93	1.75	0.21	0.86	0.49

missing mass region of $2.2 - 3.4$ GeV/c^2. From the comparison of the JAM and PYTHIA code, the error of the background level by using the different MC codes was estimated to be a factor of 2. The sensitivity of the production cross section was found to be $0.1-0.2$ nb from the simulation results.

Figure 5 shows an expected missing mass spectrum simulated by the experimental conditions. For simulating the missing mass spectrum, the calculated relative production rates which are summarized in Table II are input. In the expected spectrum, the strong dependence of the production rate can be observed. One of the subjects is to measure the production rate of the λ-mode doublet states which are enhanced in the missing mass spectrum, such as $\Lambda_c(2595)(\frac{1}{2}^-)$ and $\Lambda_c(2625)(\frac{3}{2}^-)$ and $\Lambda_c(2880)(\frac{5}{2}^+)$ and $\Lambda_c(2940)(\frac{3}{2}^+)$ for the $L = 1$ and $L = 2$ states, respectively. By taken into account the prediction from the λ-mode excitation, those λ-mode doublet states have production ratios with $R(\frac{3/2^-}{1/2^-}) \sim 2$ and $R(\frac{5/2^+}{3/2^+}) \sim \frac{3}{2}$, respectively. The measurement of the production rates of charmed baryons is expected to give one of strong evidences of the excitation modes from the diquark correlation.

III. STATUS OF THE RICH COUNTER

A. Design of the RICH counter

The cross section of the $\pi^-\ p \to Y_c^{*+}\ D^{*-}$ reaction is estimated to be at a level of nb. On the other hand, the cross section to produce at least a kaon in the final state is a few mb. A huge amount of events including K^+, π^-, π^- will be able to be reduced by identifying not only D^{*-} but also D^0. However, wrong identification of those particles increases a background level drastically. Wrong identifications of positive pions and protons with positive kaons enhances the background level in the inclusive $p\,(\pi^-, D^{*-})$ spectrum by a factor of 15 and 28, respectively. Namely, respectively only 3% of the wrong identifications of pions and protons increase the background level 2.4 times (240% increased) in the inclusive $p\,(\pi^-, D^{*-})$ reaction spectrum. Therefore, a high performance of the PID counter is essential for the charmed baryon spectroscopy.

Since the momentum range of scattered particles relevant to the charmed baryon productions is from 2 to 16 GeV/c, we designed a Ring Imaging Cherenkov (RICH) counter to identify π, K, and p for the scattered particles [15]. Two different radiators of aerogel and C_4F_{10} gas are built in the RICH counter to cover the wide momentum range. The incident and threshold momenta of the radiators are listed in Table III. At first, to check the feasibility of the counter in the simulation, we designed the RICH counter with the aerogel and C_4F_{10} radiators of 3 cm and 80 cm in thickness, respectively. By using those thicknesses of radiators, we found that enough performances were obtained by the simulation.

Then, we considered to use multi-pixel photon counters (MPPCs) for the photon sensor. Because a typical dark current rate of a MPPC is as high as 1 MHz, the accidental hit rate increases. In order to discriminate the accidental events with maintaining the efficiency for Cherenkov radiations, we need to increase the thickness of the radiators to be 6 cm and 150 cm, respectively. Those thickness of the radiators are finally determined for the actual design of the counter.

TABLE III: Information of radiators and the threshold momentum of each particle.

Radiator	n	Threshold Mom. (GeV/c)		
		π	K	p
Aerogel	1.04	0.489	1.73	3.29
C_4F_{10}	1.00137	2.67	9.43	17.9

The PID performance of the RICH counter is determined by the resolution of the particle velocity, σ_β/β. It can be calculated from $\sigma_\beta/\beta = \tan\theta \cdot \sigma_\theta/\sqrt{N}$, where θ is the Cherenkov angle, σ_θ is angular resolution and N is number of detected photons. The typical number of detected photons is $N \sim 20$ by the aerogel and C_4F_{10} radiators of 3 cm and 80 cm in thickness, respectively. The angular resolution required to separate two particles is estimated

as

$$\sigma_\theta = \frac{\sqrt{N}}{\tan\theta} \cdot \frac{(m_2^2 - m_1^2)}{2p^2 n_\sigma} \tag{1}$$

where m_1 and m_2 are masses for two particles, and p stands for a momentum of the particles. n_σ is a required distance in unit of the resolution of the measured Cherenkov angle to separate two particles. In the momentum range from 2 to 16 GeV/c, the required angular resolution is estimated to be 9.6 mrad for $n_\sigma = 5$.

Spherical mirrors are used to focus the Cherenkov photons. The radius of curvature of the mirror is chosen to be 300 cm. The mirror is located at a distance of 150 cm from the aerogel. A photon focal plane is located at the spherical surface with having a half radius of that of the mirror, where the photon detector planes are installed. Displacement of a Cherenkov photon emission point is focused at the focal plane to the first order. As shown in Figure 6, the mirrors are tilted to the beam line so that the photon detector planes are placed above and below the radiators. Photon sensors such as photo-multiplier tubes (PMTs) or MPPCs are placed at the photon detector plane. We considered that the angular resolution is composed of three components; one (σ_d) is related to a spatial resolution of the photon sensors, the second (σ_e) is from uncertainty of a emission point of a photon in the radiators, and the other (σ_m) is from optical effects such as chromatic aberrations, roughness of the mirror surface, and so on. Among these, we assume σ_e and σ_m to be 4 mrad, respectively, which are twice larger than those reported for the RICH counter operated in HERMES [16]. Then, we obtained σ_d to be $\sqrt{9.6^2 - (4^2 + 4^2)} = 7.8$ mrad. The segment size of d_{seg} is determined by the following equation,

$$d_{seg} = \frac{R \cdot \tan\theta}{\cos^2\theta} \cdot \left(1 - \frac{8}{\pi^2}\right)^{-\frac{1}{2}} \cdot \frac{\sigma_d}{\theta} \tag{2}$$

where R is the radius of curvature of the mirror. d_{seg} is 5.4 cm for $\sigma_d = 7.8$ mrad, $\cos\theta = 1/1.00137$, and $R = 300$ cm.

B. Estimation of the PID performance

1. Simulation

The performance of the PID counter is estimated by a GEANT4 based Monte-Carlo simulation. We employed a simplified geometry of placing the radiators and a photon detector plane along the beam line. Spherical mirrors are not used in this first step simulation. The thickness of the aerogel and C_4F_{10} gas are fixed to 3 cm and 80 cm, respectively. The photon detector plane is located at a distance of 200 cm from the aerogel radiator. The region between C_4F_{10} and photon detector plane is filled by air but the refraction index is set to $n = 1.00$. When MPPCs are used for photon sensors, 4 MPPCs of 3×3 mm^2 are placed in a segment of $d_{seg} = 5.4$ cm. A conical shape of light guide is attached to each

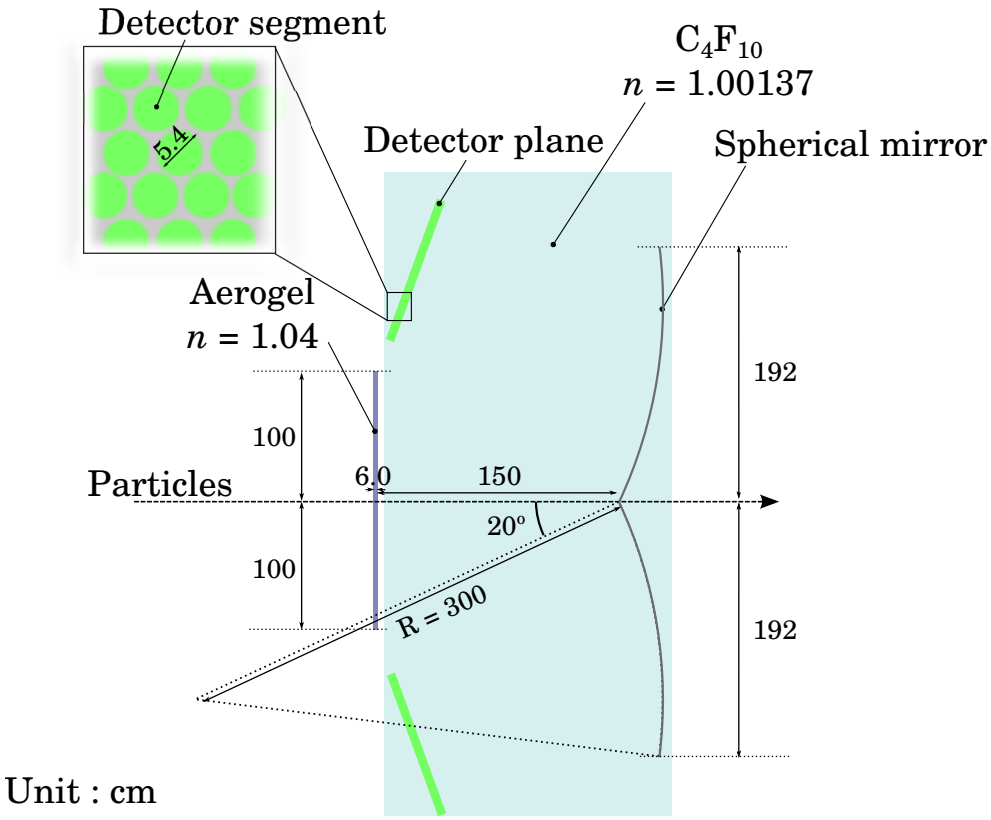

FIG. 6: Conceptual design of the PID counter

MPPC to collect photons efficiently. Collection efficiency of the light guide is estimated to be 50% by a Monte-Calro simulation. Photon detection efficiency for MPPCs are totally comparable to that for PMTs because of better quantum efficiency of MPPC. However, the dark current rate corresponding to a single photo-electron for MPPC is as high as 1 MHz, much higher than that for PMT. In order to reduce the accidental signals, the time window is restricted to 10 ns. Taking these effects in the simulation, we found that noise events are overlaid in the measured Cherenkov angle spectrum, as shown in Figure 7. As a result, the detection efficiency is reduced to discriminate the noise level. In order to recover the detection efficiency, we found that the thicknesses of the aerogel and C_4F_{10} radiators are to be 6 cm and 150 cm, respectively.

A thick radiator increases a width of the ring image, thus it may affect the angular resolution in the simulation. When the spherical mirror is used, this effect is negligible thanks to the focusing effect by the mirror. Expecting the focusing effect, we just varied photon yield and optical parameters of the radiator without changing the thickness of radiators in the simulation. Figure 8 shows the average photon angle as a function of momentum for π, K, and p. The photon angles for π, K, and p are well separated and consistent with calculated value which are drawn by gray lines in the figure.

Table IV shows the PID performance of the RICH counter. The diagonal elements show

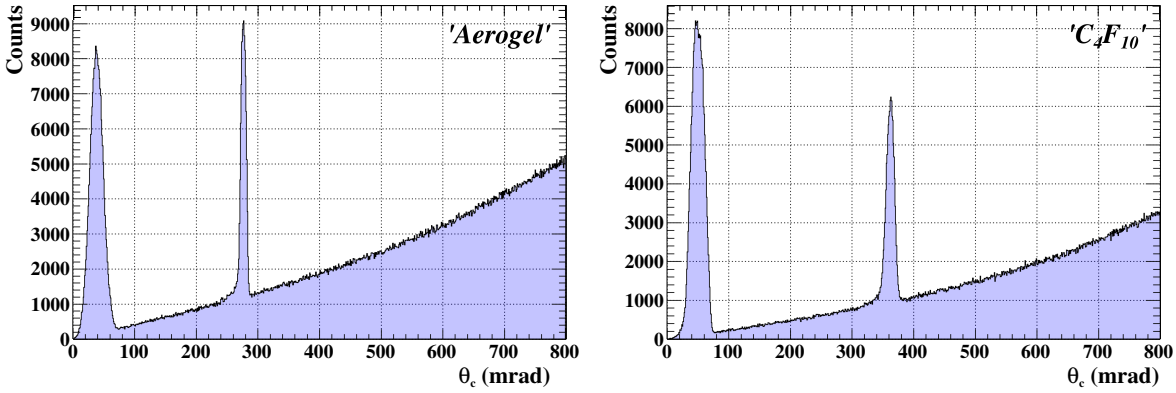

FIG. 7: Calculated Cherenkov angle distribution for each radiators. A photon angle was calculated with a emission point as center of aerogel (left) and C_4F_{10} (right).

the PID efficiencies for each particle. The other elements show wrong identification ratios. Detection efficiencies for scattered particles averaged over π and K generated by JAM are found to be 99%. Wrong identification ratios for the all particles in generated events are less than 0.5%. Then, wrong identification ratios of pions and protons to kaons which are dominant parts to increase the background in the inclusive $p\,(\pi^-, D^{*-})$ spectrum are 0.10% and 0.14%, respectively. As a results, the contribution to the background from the wrong particle identification is estimated to be 5%.

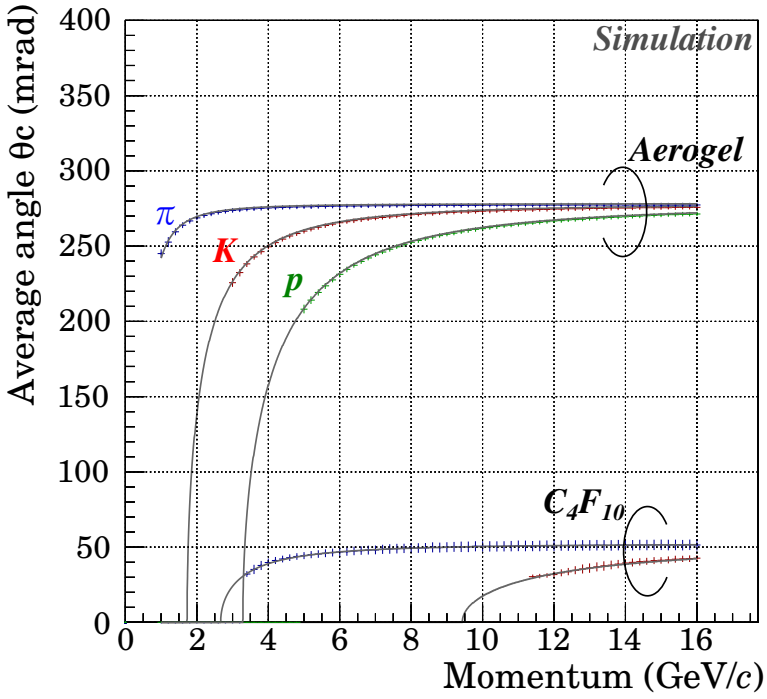

FIG. 8: Average angle of Cherenkov photons for each momentum. The blue, red and green lines show π, K and p injection, respectively. The gray line shows calculated value.

TABLE IV: The particle detection efficiency and wrong PID ratio (%)

	Incident particle		
ID as	π	K	p
π	99.5	0.85	0.02
K	0.35	98.2	0.24
p	0.16	0.64	99.0
No ID	0.00	0.33	0.78

2. Conclusion of the designed performances

The RICH counter was designed in order to identify scattered particles in the momentum range from 2 to 16 GeV/c. The RICH counter is composed of aerogel and C_4F_{10} radiators, focusing spherical mirrors and photon detection planes. Performance of the designed RICH counter was estimated by the simulation. The PID performances for π, K and p are found that the particle detection efficiencies are 99% and the wrong identification ratios of pions and proton to kaons are 0.10% and 0.14%, respectively. The contribution to the background from the wrong particle identification is estimated to be 5%. The obtained performances is satisfied to the requirements of the PID counter.

C. Test experiment of a prototype RICH counter

The PID performance of RICH counter is determined by the angular resolution of the Cherenkov angle which depends on the position resolution of the photo-detection plane. In order to obtain enough resolution with a large acceptance, it is necessary for the spherical mirrors and 2 pieces of photo-detection plane which have size of 2.0×1.0 m constructed by more than 2000 photon sensors. We plan to use the multi-pixel photon counter(MPPC) as a photon sensor. The MPPC can detect 1 photon with good separation which is advantage to detect feeble Cherenkov photons. In addition, it is not affected by the magnetic field near the spectrometer magnet as compared to the PMT. However, it is expected that a larger dark current rate of MPPC which is typically 100 kHz/mm^2 increases noise hit. Consequently, the PID performance may become worse. For studying the performance of the spherical mirrors and the MPPC detector plane, the test experiment was performed by using an electron beam at the GeV-γ experimental hall in the Research Center for Electron Photon Science (ELPH). The electron beam is suitable to study the response of the the spherical mirrors and the MPPC detector plane because the Cherenkov angle can be fixed as the same value due the particle velocity (β) which can be assumed to be 1. The preliminarily results are reported.

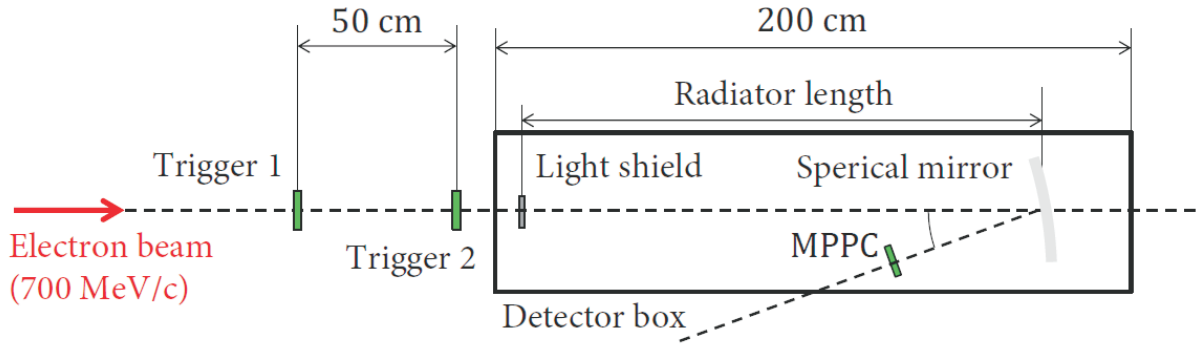

FIG. 9: Schematic view of the setup.

FIG. 10: Prototype RICH counter. (left) Detector box of the Prototype RICH counter. Electron beam comes from left side. (middle) MPPC photo-detection plane. MPPC is mounted on the readout board. (right) Spherical mirror.

1. *Experimental setup*

Electron beam which has momentum of up to 700 MeV/c was induced to a prototype RICH counter. Electrons which passes the center of the counter is selected by trigger counters located upstream and down stream of the prototype RICH counter. As shown in Fig. 9, the prototype RICH counter contains a MPPC photo-detection plane and a focusing spherical mirror (each part shown in Fig. 10). All counter components are installed to the back-painted box for shielding light. We used the S12642-0808 module made by Hamamatsu Photonics which has 64 segments (8×8) and each segment size is 3.1×3.1 mm^2. The total detection area is 25.8×25.8 mm^2. The spherical mirror is used for focusing the Cherenkov photons and transferring photons to the MPPC photo-detection plane. The curvature radius of mirror is 330 mm which was determined by the size of photo-detection plane. The reflection surface is made by Aluminum which has reflectance of $\sim$90% in the visible light. Air was used for radiators which have refractive indices of 1.000293.

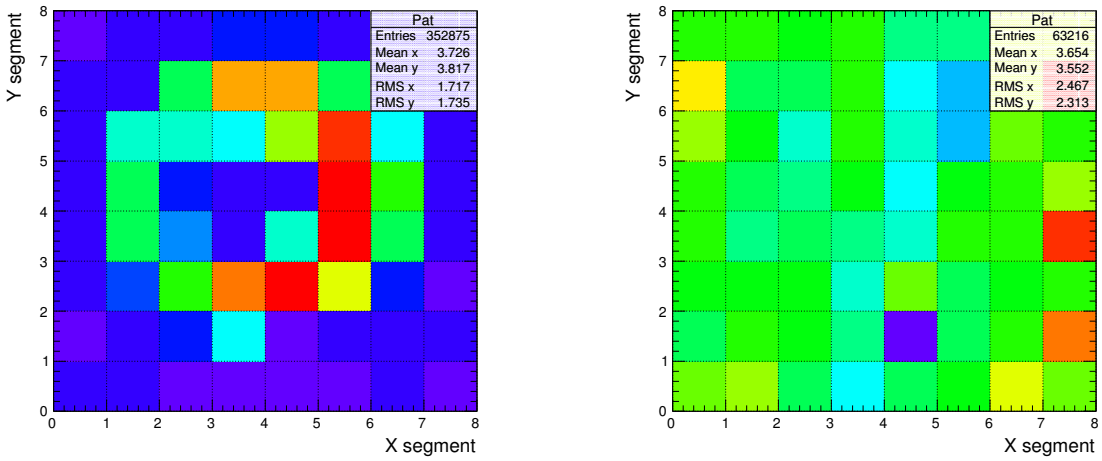

FIG. 11: Hit pattern of photon-detection plane. (left) Cherenkov region is selected. The Cherenkov ring is clearly observed. (right) Dark current region is selected. There is no ring structure.

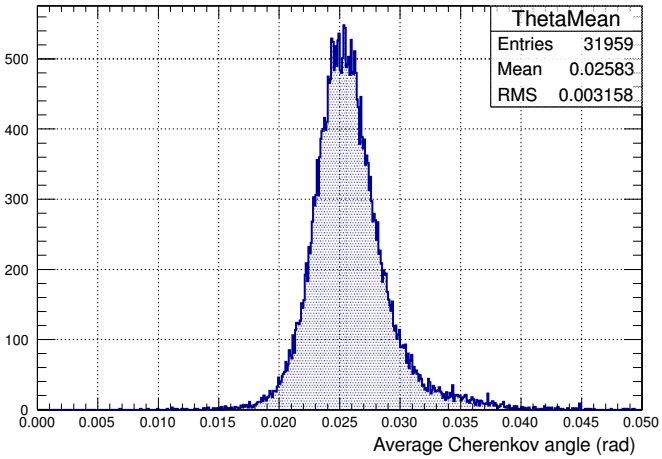

FIG. 12: Average Cherenkov angle distribution. A peak from Cherenkov photons is clearly observed around 25 mrad.

2. Experimental results

The hit pattern of photon-detection plane is shown in Figure 11. The Cherenkov ring can be observed and S/N ratio become better by selecting the Cherenkov peak from the timing information. The Cherenkov angle is calculated by simple equation,

$$\theta_c = \mathrm{Tan}^{-1}\left(\frac{R_{ring}}{R_{mir}}\right), \tag{3}$$

where R_{ring} and R_{mir} are radius of the Cherenkov ring and spherical mirror, respectively. All positions of the detected photons in one triggered event are converted to the Cherenkov angle. Then, all of the potions are averaged to determine the Cherenkov angle. Figure 12 shows the Cherenkov angle distribution. There is clear peak around 25 mrad which corresponds to $\theta_{Air} = \mathrm{Sin}^{-1}(1/\beta\ n) = 24$ mrad, where β is particle velocity which is fixed 1.0 and n is refractive index of air. The angular resolution is extracted to be 3.0 mrad. The effect from effects from dark current noise is found to be small.

3. Summary of the preliminary result

A prototype RICH counter with a MPPC photo-detection plane was tested by using the electron beam. The Cherenkov angle and its angular resolution was measured at different beam momenta, mirror angles. Clear Cherenkov ring images were observed with a typical angular resolution of 3.0 mrad. Since the present analysis is still preliminarily, more detail analysis is ongoing.

IV. STATUS OF THE HIGH-RATE COUNTERS

The intense π^- beam of 6.0×10^7/spill (30 MHz for the 2 sec extraction) is planned to be used in the experiment. The production cross section of the charmed baryon is expected to be small. It is essential for the experiment to use the intense beam. This beam intensity is over the limit of the wire chamber operation so that high-rate detectors are needed to handle the beam. For beam measurement, a high-rate counters, such as a scintillating fiber tracker and a silicon strip detector, will be installed. The reference timing is also measured by a fine segmented timing counter. The high-rate capability of those counters is needed to be satisfied under the operation by assuming the beam with size of 100×100 mm^2 and expecting total counting rate of 30 MHz. In this section, the concept to measure the high-rate beam is reported.

A. Beam measurement with present time structure of beam

For the experiments at the hadron facility, a uniform beam within an extraction period should be supplied to the experimental area. In the case of the present J-PARC, the beam orbit in MR is not stable and the extracted beam has a non-uniform time structure. It has pulse-like structure with intensity busts which are much higher than the flat distribution. Thus, counting rates of timing counters and tracking detectors often exceeded the limit of their operation. Accordingly, the beam intensity was precisely adjusted within the operational level. In the present experiment, an effective extraction time length over the extraction time called duty factor is 30$\sim$40%. The duty factor is being improved run by run of the slow extraction beam time. However, the instantaneous rate still exceeds the limit of the detector operation when we use the high-rate beam. Therefore, we should take into account not only the high counting rate beam but also the bad time structure for the measurement of the high-rate beam.

For operating the high-rate beam, past experiments give us information and experience how to overcame difficulties. The high-rate pion beam was used for the past experiment, J-PARC E10 [17], at the K1.8 beam line. In the experiment, the intense pion beam of 12 M/spill (6 MHz for the 2 sec extraction) was used. For measuring the pion beam, we replaced the tracking detectors to the high-rate ones as shown in Fig. 13, in particular, at the places where the counting rate exceeded the limit of previously installed tracking detectors. The scintillating fiber tracker with one layer configuration was installed at the most upstream part of the beam line spectrometer at the K1.8 beam line because the most upstream part has very high counting rate environment. We also installed the scintillating fiber tracker with three layers at the downstream of the experimental target where the beam was focused so that the counting rate per one detector segment was high. In addition, at the upstream of the target, we installed the silicon strip detector to measure precise vertex positions. We

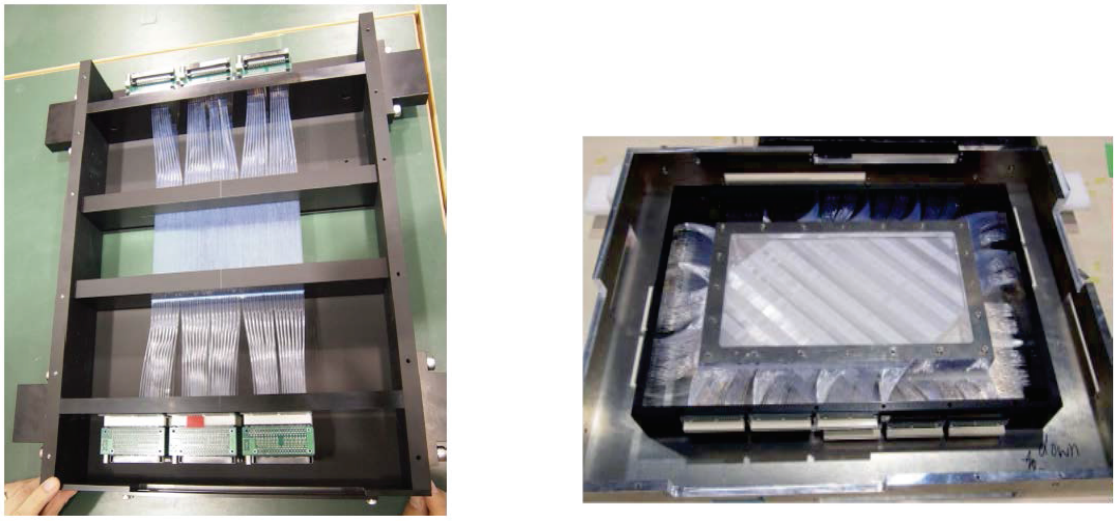

FIG. 13: Scintillating fiber trackers installed for the J-PARC E10 experiment at the K1.8 beam line. The scintillating fiber tracker installed at the most upstream part of the beam line spectrometer(left) and at the downstream of the experimental target(right) are shown.

could not replace all the detectors to the high-rate one. The conventional drift chambers with a 1.5-mm and 2.5-mm drift spacing were used by combining the high-rate detector. For analyzing those high-rate beam, we developed a new tracking routine by combining the hit position of the timing counters. The density of the counting rate is localized in the short period by considering the bad time structure. The multi-track events could not be rejected by only using drift chambers which had a wide time gate of the drift time. By combining the hit position between the timing counters and reconstructed tracks, we could suppress the fake tracks due to the accidental hits of drift chambers. Consequently, the true track events can be obtained from the new tracking routine. Using those high-rate detector and tracking analysis method, we could use the beam intensity of more than 10 M/spill which could not be treated by using only the conventional tracking detectors such as MWPCs and drift chambers.

The most important point of the previous E10 experiment is to measure the high-rate beam with a "narrow time gate". Figure 14 shows the time gates of the scintillating fiber tracker and the drift chamber with a 1.5-mm drift spacing in E10. The drift chamber needed a time gate of $\sim$50 ns, while the scintillating fiber tracker was $\sim$1 ns. It is obvious for the rejecting power of the accidental beam hits. In addition, in the E10 experiment, all tracking detectors were not replaced to be high-rate ones. By replacing all detectors, more high-rate beam could be used because the scintillating fiber detectors were not reached to its operation limit. Therefore, it is a key to use a high-rate detector having a fast time response for a narrow time gate which enables us to measure the correct tracking events. For the E50 experiment, a set of high-rate detectors are essential for the beam measurement.

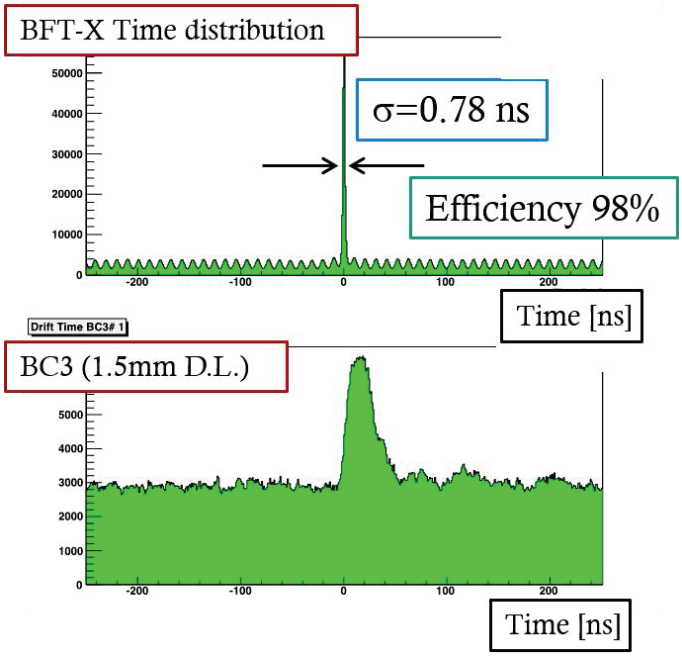

FIG. 14: The distributions of the timing information of the scintillating fiber tracker(upper) and the drift chamber(bottom). The drift chamber needed a time gate of ∼50 ns, while the scintillating fiber tracker was ∼1 ns.

B. Choice of high-rate tracking detectors

For the E50 experiment, the high-rate detectors have to be installed at the region where beam pass though. The choices of high-rate tracking detectors are discussed.

1. Focal plane and target upstream

In the region of the focal plane and the target upstream, the focused beams of 100×100 mm^2 are measured by the tracking detectors with a multi-layer configuration. The counting rate per 1 mm segment is expected to 0.3−1 MHz from the total intensity of 30 MHz. As discussed in previous section, this counting rate exceeds the limit of the operation of drift chamber. It is essential to use for the high-rate detectors such as a scintillating fiber tracker, silicon strip detector(SSD) or GEM.

From the point of view to measure beam with a narrow time gate from the results of the E10 experiment, the scintillating fiber tracker is one of the best candidates of beam tracking detectors. The scintillating fiber is capable to select hit events with a 1-ns gate width. Also, the scintillating fiber tracker had successfully been used in the J-PARC E10 experiment so that there are knowledge and experience how to operate it in the high-rate environment. The disadvantage of the scintillating fiber tracker is its material thickness. The development

with the thin scintillating fiber is one of the issues for the detector development. We plan to use MPPC as a photo-detector from fibers. The development of the readout module is also important work. The readout module is discussed in Sec. VI.

SSD is has a fine segment which suppresses the counting rate per one segment to be low. However, from the result of the E10 experiment, the hit multiplicity of each plane could not be suppressed because we could not measure each hit with the narrow time gate [18]. The slower time response than the that of scintillating fiber is a disadvantage of SSD. For measuring the beams with 100×100 mm^2, the development of suitable size SSD is issue. If the smaller size SSDs than that of beam are used by overlapping each layer, the material thickness become thicker and nonuniform in the region of beam passing through.

GEM has the same feature as of SSD, such as fine segmentation and slower time response. There is advantage that we can produce suitable size for covering the beams with 100×100 mm^2 and GEM is capable to use the high counting rate which corresponds to 5 kHz/mm^2. The disadvantage of GEM is thicker material thickness than that of the scintillating fiber and SSD.

From those points, for the measurement of the high-rate beam, we choose the scintillating fiber tracker as a beam line tracking detector. However, SSD and GEM have good spatial resolution and good readout electronics which are developed by other experimental groups. Those detector can be combined to the scintillating fiber tracker for improving the spatial and vertex resolution. The additional installation of SSD or GEM with a few layers at the upstream and downstream of the experimental target can be possible for measuring the vertex position with a good spatial resolution. For the first stage of development, we concentrate to develop the scintillating fiber tracker as a beam line tracking detector.

2. Target downstream

At the downstream of the target, the tracking detectors have to be operated under the conditions of both the high-rate beam and the high-rate scattered particles because the regions of the beam and scattered particle are overlapped. The total charged particle cross section of the π^- p reaction measured at the beam momentum of 16 GeV/c [19]. From the cross section values in Ref [19], the multi-track rate with averaged particle number of 4 tacks is estimated to be 3.6 M/spill by the expected experimental conditions (4 g/cm^2 target, 6.0×10^7/spill beam). In this condition, it is expected for the incorrect tracking from both the accidental tracks and the wrong tracking connection between tracks measured by set of tracking detectors at the downstream of the target and inside the spectrometer magnet. In addition, the tracking detectors at the downstream of the target should cover a wide area because tracking detectors have to measure scattered particle with a wide angular range from both the charmed baryon production and decay events. It is necessary to install tracking detectors to avoid the incorrect tracking and to cover a wide area.

In the case of the E10 experiment, at the downstream of the target, we installed the scintillating fiber tracker and drift chamber with a 2.5-mm drift space. Both detectors could be operated in the high-rate beam without losing their hit efficiencies, while the drift chamber had large accidental hits at the region where the beam passed trough. During the track solving process in the analysis, the accidental beam hit events from drift chamber could not distinguish from the true scattered particle events. However, by combining the event from the scintillating fiber tracker for gating the narrow timing gate in the analysis process, we could clearly separate the true tracks from scattered particles. The accidental events were almost suppressed by gating the narrow timing gate. It is found that the scintillating fiber tracker for gating the narrow timing gate is a key method.

To avoid the incorrect tracking and to cover a wide area, the redundant tracking system is much effective for the tracking at the downstream of the target. Two kinds of the tracking detectors are installed for solving correct tracks, the scintillating fiber tracker with a large size for gating the narrow timing gate and the internal drift chamber for covering a wide area. By combining those tracking detectors, it is possible to measure the multi-particle tracks under the high-rate condition without the incorrect tracking by keeping the acceptance. The scintillating fiber tracker and drift chamber can cover wide area for detecting scattered particles. The high-rate tracking system by using both the scintillating fiber tracker and drift chamber is one of the key detector for the experiment.

C. Development items

The list of developing the high-rate counter is shown as follows.

- Simulation of the accidental hit rate by using the actual time structure of the preset J-PARC beam.
- Simulation and determination of the fiber shape and size by taking into account the multiple scattering effect and energy loss effect for mass resolution.
- High-rate test of the scintillating fiber trackers, a 1-mm size circle fiber for which the photo-sensor and readout electronics are 1-mm MPPC and EASIROC, respectively.
- Choice of MPPC: Small pixcel sensor.
- Test production of large size scintillating fiber tracker (600×800 mm^2) to check how to make a straight and flat fiber layer by using a large size frame.
- Development of readout electronics: Show DAQ section.
- Possible combination with other high-rate tracking detectors such as SSD and GEM.

V. STATUS OF OTHER DETECTORS

A. Time definition counter

The experiment by using the random trigger is necessary to determine the time reference (time zero) in event by event because there are no synchronized information such as the accelerator RF for the collider experiment. For determination of the time zero, the time definition counter (time zero counter) will be installed. In the conventional fixed target experiment, the time zero counter is installed at the upstream of the experimental target due to no fluctuation of the timing determined by the beam with an uniform momentum. We can also measure the time zero from the scattered particles, but this method makes it difficult for analyzing the events because it is necessary for the correction of the timing of all the detectors event by event according to the detected particle momentum, the path length of tracks and the pulse height by energy deposit by a different velocity. It is reasonable to install the time zero counter for measuring the beam timing as a reference.

On the other hand, for the high-rate beam experiment, it is difficult to operate the time zero counter in the high-rate beam. The time zero counter is required to have a good time resolution less than 100 ps(rms), while the its timing signal should be stable for determining the timing of the trigger for many experimental apparatus. For satisfying the requirements, we plan to develop the time zero counter(T0) for the high-rate beam. In the present study, the combination of a fine segmented plastic scintillator and MPPC can be possible solution for T0. The expected counting rate of the central segment is 3 MHz for the segment size of 3 mm connected to the 3-mm squared MPPC. MPPC has good intrinsic time resolution of less than 50 ps(rms) so that the light yield of the connected plastic scintillator is needed to be studied. For confirming the performances of T0, the test measurement by changing the light yield of the plastic scintillator (actually the length of scintillator is changed) and the test experiment by using high-rate beam is planned.

B. Wire chamber

For the tracking detectors at the downstream of the target, inside of the magnet gap and downstream of the magnet, a large size detectors are needed for covering large areas. For this purpose, conventional drift chambers or straw tube chamber are candidates because the counting rate per each wire is low enough except for the region where beam pass through. As shown in Fig. 15, we plan to install the conventional drift chambers or straw tube chambers to the spectrometer system as follows.

- Target downstream DC: Planer type chamber with tile wires, cell size of 5−10 mm
- Internal DC: Cylindrical type chamber with stereo wires, cell size of 10−20 mm

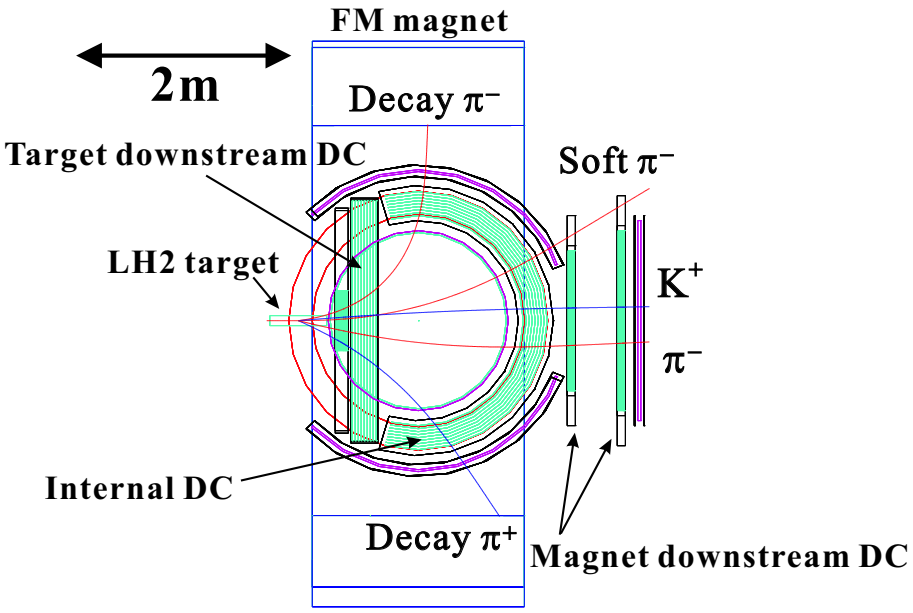

FIG. 15: Wire chambers installed to the spectrometer.

- Magnet downstream DC: Planer type chambers with tile wires, cell size of 10−20 mm

The cell structure and size are being studied. In addition, the choice of drift chamber or straw tube chamber is also being studied by checking the multiple scattering effect for scattered particles. The number of the layer will be determined for keeping the redundancy to reconstruct the multi tracks of scattered particles.

C. Counters for timing measurement

1. TOF counter

TOF counter is installed at the downstream of the spectrometer magnet between the drift chamber and the scattered particle RICH. Because the particle identification by the Time-Of-Flight method is difficult for the high-momentum particle with 2-16 GeV/c, the role of the counter is to determine time reference for the downstream drift chamber and RICH. The size of counter is 2.0×1.8 m^2, which is segmented by 50 mm with both side readout. The typical counting rate at the high-rate region except for beam region is estimated to be 300 KHz. The counting rate is acceptable so that the conventional plastic scintillators and photo-sensors such as PMT are available. For the beam region, we plan to give up to readout both size, while the segment is divided in to upper and bottom ones. Then, we plan to additionally install the fiber or fine segmented timing counter for keeping the acceptance.

2. Internal TOF counter

In the magnet gap, the internal TOF counter(ITOF) will be installed inside of the spectrometer magnet. The function of ITOF is to identify scattered particles having a momentum of less than 1.7 GeV/c, and to determine the time reference for the internal drift chamber. For the particle identification of scattered particles by the Time-Of-Flight method, the required time resolution is less than 70 ps(rms) for the maximum momentum. The Resistive Plate Chamber is a candidate of ITOF. The counting rate of ITOF installed near the side wall of the magnet is low enough to operate RPC (less than 1 kHz/cm^2). RPC is developed by the LEPS group [20] so that the E50 group can collaborate them for developing the RPC counter.

3. Pole face TOF counter

In the magnet pole face, the pole face TOF counter(PTOF) will be installed for detecting particles which are scattered to the magnet pole face, such as from the charmed baryon decay events. Particles scattered to the vertical direction also make tracks to the target downstream trackers. To install the timing counter on the magnet pole face, we can detect those scattered particles. The acceptance of the azimuthal angle can also be covered by PTOF. Those particles have a momentum of less than 1.2 GeV/c, while the flight path is short. Therefore, the required time resolution is less than 70 ps(rms) for the maximum momentum for the particle identification. The Resistive Plate Chamber is a candidate of PTOF.

VI. STATUS OF THE DAQ SYSTEM

A. DAQ overview

Figure 16 illustrates a conceptual schematic of the DAQ system. Detector signals are digitized on front-end electronics modules placed near the detectors with a pipelined data transfer. A raw data size of ∼40 GB/spill is roughly expected for the beam rate of 60 M/spill. The data of front-end modules are transferred by a self-trigger (or a periodic trigger) via FPGA's build-in multi-gigabit transceivers and/or 1G/2.5G/5G/10G Ethernet to buffer PCs. The PC nodes at the first stage plays as buffers and load balancers, which store the data and switch a destination of the data spill by spill. The PC nodes at the second stage plays as event filters. Each filter node performs the cellular automaton tracking, analyzes the RICH data (clustering and/or image reconstruction), scaler counting and writes the data into the local storage device. A part of data are visualized on monitoring PCs. Since the price of several tens to a hundred GB memories becomes not so expensive nowadays, each node can be equipped with an enough memory to store the whole data of one spill. The recorded data are forwarded to the KEKCC storage and the computing farm at RCNP. The filter nodes, local storages and monitoring PCs are placed at the counting room, whereas the buffer nodes are located at the experimental area. The experimental area and the counting room are connected with high speed optical links (10G/40G Ethernet, InfiniBand, etc.) in order to cope with ∼40 GB/spill data rate, which corresponds to ∼70 Gbps after the derandomization.

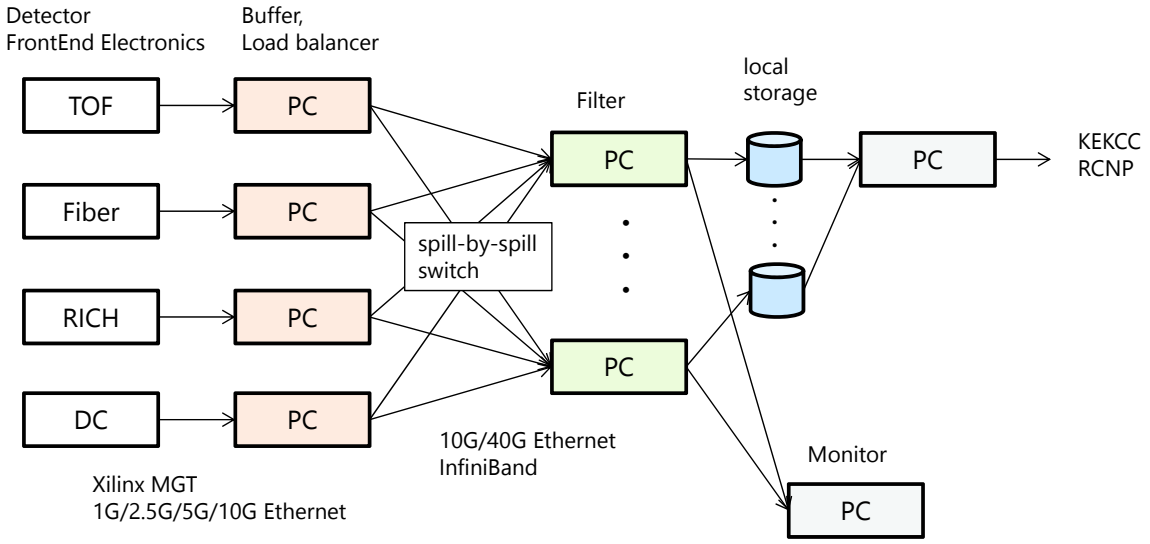

FIG. 16: A conceptual view of DAQ system.

B. Trigger

Table V summarizes a trigger rate estimation, assuming that the liquid hydrogen target with the thickness of 4.0 g/cm^2 is bombarded by π beam with the intensity of 60 M/spill. A typical charged track multiplicity is 4 for each reaction. A simple coincidence of the timing counter (trigger condition C1 in Table V) only reduces the rate from 3.6 M/spill to 1.1−2 M/spill. A reduction of more than one order of magnitude needs the RICH information (trigger condition C2) and/or the tracker information (trigger condition C3) whose number of channels are ∼10,000 and ∼8,000, respectively. Signal processing of such large number of channels is very complicated for the traditional hardware based trigger system even if large scale FPGAs are employed.

The present document proposes the different approach, which uses a commercial CPU cluster for the on-line trigger decision in the similar way of the CBM on-line computing. The CBM experiment at FAIR demonstrates the performance of their first level event selection (FLES) package for simulation data, which utilizes a many-core CPU/GPU farm [21]. A cellular automaton track finder and a Kalman filter based track fit are massively parallelized in the FLES package. They achieved the track reconstruction rate of faster than 100 μsec/track/physical-CPU-core, with Intel Xeon E7-4860 CPUs. Assuming the same level of the track reconstruction performance, 60k tracks/core is expected for the 6-seconds spill of the J-PARC slow extraction. In order to satisfy the E50 requirement, where 1.1−2 M×4 = 4.5−8M tracks/spill must be reconstructed for the events after the C1 condition filter, 100-200 CPU cores are needed. The feasibility and optimization including a utilization of the many-core hardware accelerators/co-processors (Intel Xeon Phi, NVIDIA Tesla GPU, etc.) will be studied.

TABLE V: Trigger rate estimation. LH2 target thickness of 4.0 g/cm^2 and 2-seconds spill per 6-seconds cycle are assumed.

		/spill
Beam		60M
Reaction		3.63M
	trigger condition	/spill
C1	[TOF≥2] ⊗ [ITOF(negative)≥1]	1.1M–2M
C2	C1 ⊗ [SFT ≥3] ⊗ [RICH = π] ⊗ [AC = K or proton (p >3 GeV/c)]	160k
C3	C2 ⊗ [Momentum analysis (DC, Fiber)]	15k–23k

C. Timing synchronization

A global clock is distributed from the Belle-II FTSW(Fast Timing SWitch) [22]. The clock jitter of 30 psec (RMS) is acceptable for E50. Trigger data packets inform the spill On/Off, calibration start/stop, reset signal and so on.

D. Front-end electronics

Common requirements for the front-end electronics modules are as follows.

- Time stamp synchronization by the global clock.
- Basically, TDC is used for all of the detector signal digitization. Time stamps of hit pulses and their time-over-threshold (TOT) are recorded. The TOT is mainly used for a slewing correction of the time measurement.
- Data through put at least 1 Gbps per module. 4–5 Gbps is needed for readout modules of a beam detecting plane.
- No dead time.
- Self triggering or periodic triggering.
- Keep it simple.

The current plan and performance requirements on a rate capability and time resolution of the readout electronics are summarized in Table VI.

TABLE VI: Summary of front-end electronics.

Detector type	# of ch.	rate [MHz/ch]	time resolution [nsec] (σ)	Front-end	TDC LSB [nsec]
Sci.Fi.	9600	1	< 1	MPPC with CITIROC or PETIROC2	1
RICH	10500	0.1	< 1	MPPC with CITIROC	1
beam TOF	140	3	< 0.1	MPPC with PETIROC2 or discrete amp	0.025
TOF	160	0.30	< 0.1	FM-PMT	0.025
RPC	184	<0.01	< 0.1	Discrete amp	0.025
DC	7545	0.20	< 1	DC-FEAT	1

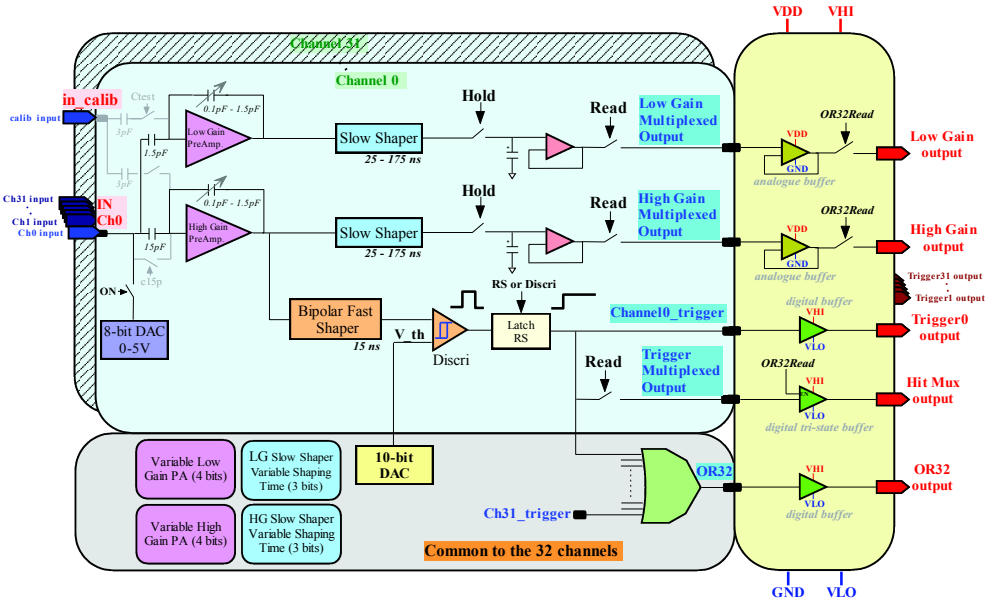

FIG. 17: A block diagram of EASIROC [25].

E. MPPC readout

Considerable number of MPPC will be used in E50 for readout of scintillation fiber trackers, ring imaging Čerenkov counters and timing counters. For a multi-channel MPPC readout, EASIROC [23] has been successfully used by many groups. However, existing EASIROC modules (evaluation board, NIM and VME) do not have a high through put data link. In addition, its pulse width is not so short and it has been empirically found that inefficiency appears when hit interval goes to less than 300 nsec. Therefore, development of a new module with multi-gigabit transceiver is needed and the alternative front-end electronics for the MPPC should be researched. Requirements and candidates are summarized in Table VI. The fiber trackers must be cope with 1 MHz/ch even for a 1-mm thickness fiber. The requirements for the beam timing counter, which is a 3-mm wide plastic scintillator slab, are not only high rate capability of 3 MHz/ch, but also the single counter timing resolution of better than 100 psec (σ). Two candidate chips, CITIROC and PETIROC2 [23], are available from the same group who designed EASIROC. Block schemes of EASIROC, CITIROC and PETIROC2 are shown in Figs. 17,18,19.

CITIROC is a successor to EASIROC. Improved features of CITIROC from EASIROC are as follows.

- Channel-by-channel uniformity of input DAC : 3% $\rightarrow$ 1%.
- Timing jitter of the trigger out (discriminator output of the fast shaper) : 60–70 psec (σ)

Those features are preferred for fiber tracker readout as well as RICH readout.

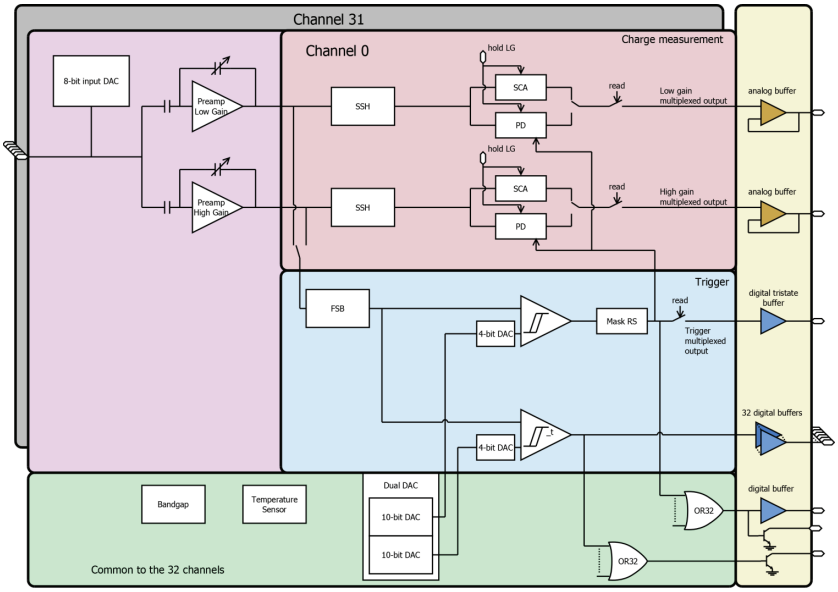

FIG. 18: A block diagram of CITIROC [26].

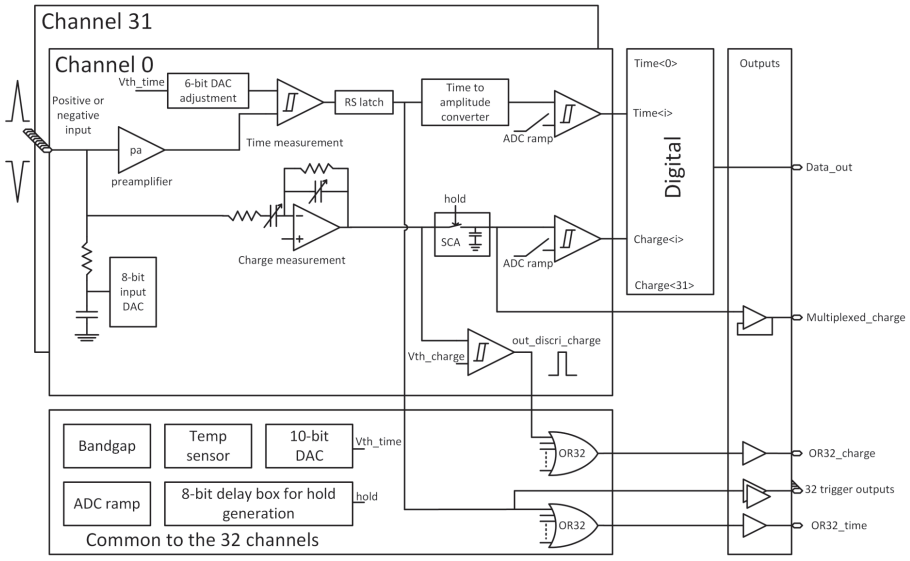

FIG. 19: A block diagram of PETIROC2 [27].

PETIROC2 is a 32-channel front-end ASIC designed for particle time-of-flight measurement with MPPC. PETIROC2 contains a wide band preamplifier (877 MHz bandwidth). The output signal of the preamplifier is very sharp, whose width is less than 10 nsec. The time jitter of the discriminator output is ∼20 psec for charge injection bigger than 3 p.e. (photoelectron). The short pulse is very attractive for both the fiber tracker and timing counter readout. The drawback of PETIROC2 is low sensitivity of a single photon measurement as shown in Fig. 20, which requires additional study for gain adjustment of the MPPC.

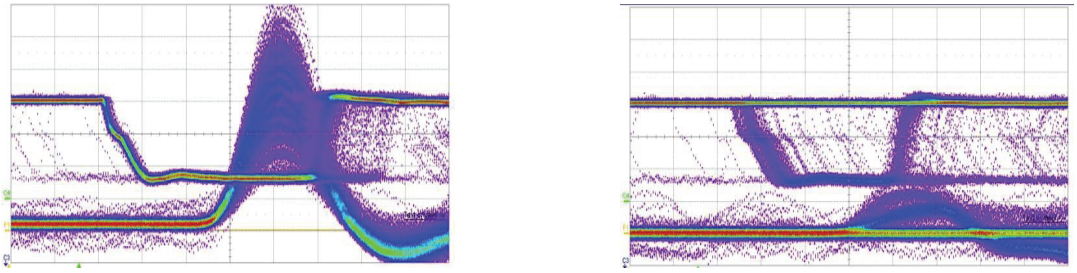

FIG. 20: Pulse shapes of the preamp out and trigger out of the PETIROC1 (analog version of PETIROC2) [28]. Input photoelectron is injected by a laser pulse. (Left) 10 p.e. laser injection with 5 p.e. trigger threshold. (Right) 1 p.e. laser injection with 0.5 p.e. trigger threshold. Vertical grid lines are drawn with 2 nsec per step.

In 2015, the performance check of the two chips will be performed. The development of the chip evaluation board is ongoing. The evaluation board consists of two parts, one is an analog card which contains ASICs, the other is a digital card on which a FPGA and ADCs are mounted. A multi-channel TDC with 1 nsec LSB will be implemented in the FPGA using multi-phase clock sampling technique or built-in SerDes (Serializer-Deserializer) to measure the leading edge and the TOT of input signals. ADCs are used for the precise charge measurement and fine tuning of the bias voltage of MPPCs.

The large TOF counter at forward is read by fine-mesh PMT (FM-PMT). Since the counting rate is moderate of 300 kHz/ch, such a conventional method can be applied. On the other hand, R&D of readout circuit for the TOF measurement with MPPC is most challenging. Figure 21 shows a pulse width dependence of hit loss probability for several hit rates. The blue and red lines correspond to 1 MHz and 3 MHz, respectively. In order to keep a detection efficiency more than 99% for each channel, the discriminator output pulse must be less than 10-nsec (3-nsec) width for a 1-MHz (3-MHz) hit rate. Even a 10-nsec width pulse is suffered from a 2.6% loss at a 3-MHz hit rate.

Applications of MPPCs to a timing counter made of a plastic scintillator have been reported [29], [30]. Figure 22 shows the circuit diagrams of the amplifier board of MEG-II and ELPH groups. MEG-II group [29] used a series-connected MPPC array. Three MPPC elements (3×3 mm^2 each) were attached for the readout of a plastic scintillator, whose size is $60 \times 30 \times 5$ mm^3. Advantages of the series connection are automatic adjustment of over-voltage among the MPPC array and narrower pulse shape due to the total capacitance reduction. Disadvantage is that higher bias voltage is needed and that the signal size is reduced. In their case, the signal of the 3-MPPC series is one third compared to a single MPPC. The pulse shape of the MEG-II readout electronics is shown in Fig. 23. They analyzed a waveform sampled by DRS4 and obtained a resolution of $\sigma = 42 \pm 2$ psec at 1 MeV energy deposition. On the other hand, ELPH group [30] used a parallel-connected MPPC array. A $10 \times 12.6 \times 24$ mm^3 counter was read by 16 MPPC elements (3×3 mm^2

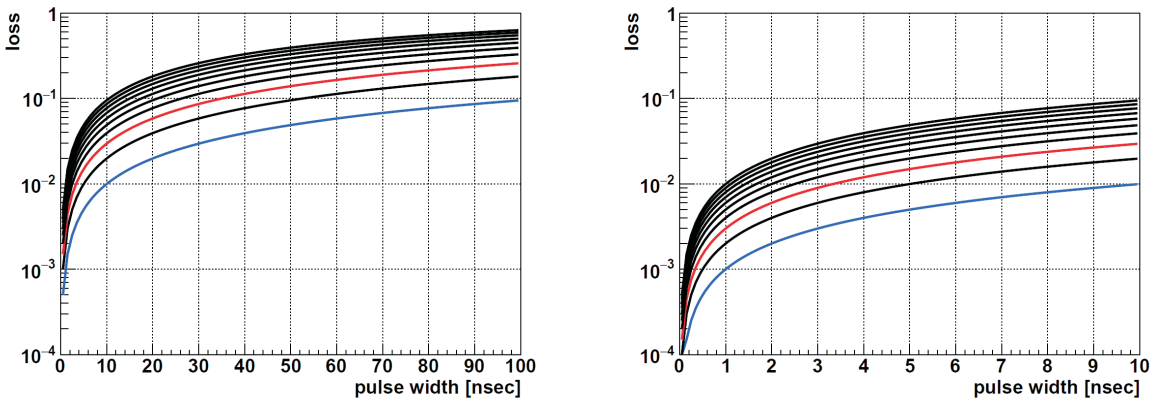

FIG. 21: Pulse width dependence of hit loss probability. The probability is calculated as $1 - e^{-(rate)\times(pulse-width)}$ with a step of 1 MHz rate from 1 MHz to 10 MHz. The blue and red lines correspond to 1 MHz and 3 MHz, respectively. The right panel shows a zoom of the left panel.

each). An advantage of the parallel connection is that the output of the MPPC array can be summed up, which brings a large signal. Disadvantages are that the large capacitance makes the decay time of the output signal longer, that the dark counts of all the sensors are also summed up and that the bias tuning is a complicated task for a large number of channels. In order to recover the high slew rate, a high-pass filter was implemented at the input stage of the circuit developed by ELPH group, which is shown in Fig. 22. The pulse shape of the ELPH readout electronics is shown in Fig. 24. They obtained a resolution of $\sigma \sim 60$ psec at a MIP energy with CAEN's high resolution TDC (V775) and QDC (V792). At the start point of the R&D for the front-end electronics of the E50 TOF, the same discrete circuit as that of ELPH and PETIROC2 will be tested. MPPC array connection in series or parallel will also be tested to study the readout method alternative to FM-PMT for the large TOF counter readout.

Development of a high resolution TDC is also the challenge for E50. HPTDC (High Performance Time to Digital Converter) developed by CERN [31] is not suitable for E50 TOF measurement because of data loss at high rate. The recommended maximum hit rate of HPTDC running in very high resolution mode (LSB = 25 psec, 8 ch/chip) is 2 MHz/ch (4 MHz/ch) with a 40 MHz (80 MHz) clock [32], otherwise hit loss occurs. In addition, recommended maximum trigger rate is 500 kHz. It is highly possible that the hit rate of beam TOF counter of E50 exceeds the limit. Therefore, development of a new high resolution TDC using FPGA is planned. The FPGA-based high resolution TDC utilizes a carry chain and flip-flops as a tapped delay line. A precise time measurement between a coarse counter clock is interpolated by the tapped delay line. HADES group has developed a $256 + 4 + 4$ channel high resolution TDC module based on this scheme with 4+1 Lattice FPGAs (TRB3, TDC Readout Board v3) [33], [34] in order to replace a HPTDC module. The achieved performances of TRB3 were typical 7.2 psec RMS time resolution on a single

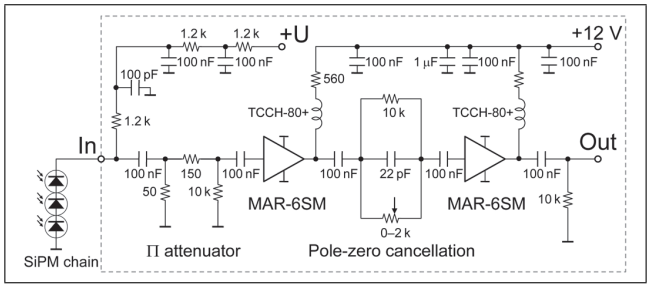

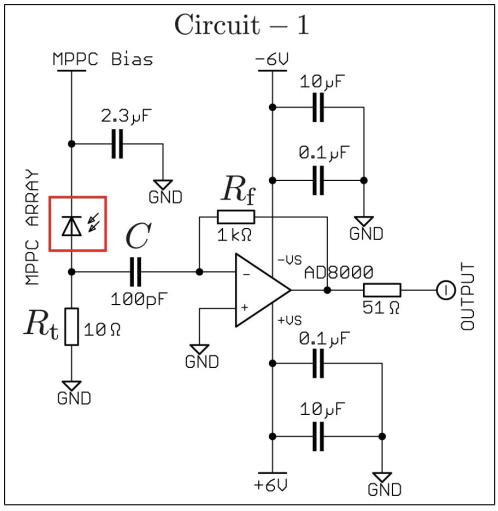

FIG. 22: Circuit diagrams of the amplifier board for MEG-II (left) [29] and ELPH (right) [30]. Wide bandwidth amplifier MAR-6SM (2 GHz bandwidth) and AD8000 (1.5 GHz) are used in the MEG-II board and the ELPH board, respectively.

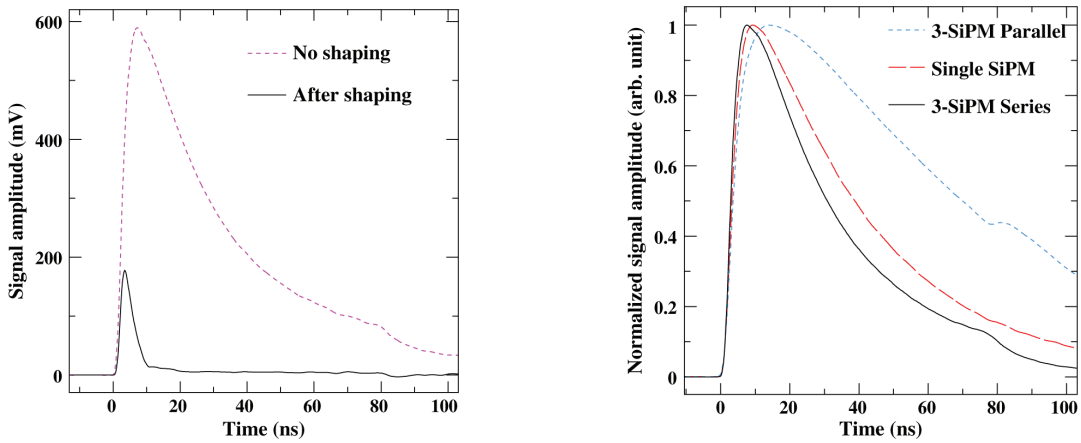

FIG. 23: Pulse shape comparison of the MEG-II MPPC readout [29]. (Left) With (solid line) and without (dashed line) the analog shaping. (Right) Pulse shape difference for different MPPC connections. These pulse shapes correspond to those without the analog shaping.

channel, 66.7 MHz hit rate per channel and maximum trigger rate of 700 kHz trigger. A similar module to TRB3 will be built by E50.

F. RPC readout

A current plan of RPC readout electronics is that it is composed of discrete broadband preamplifiers, discriminators and high resolution TDC modules. R&D will be done with LEPS2 group.

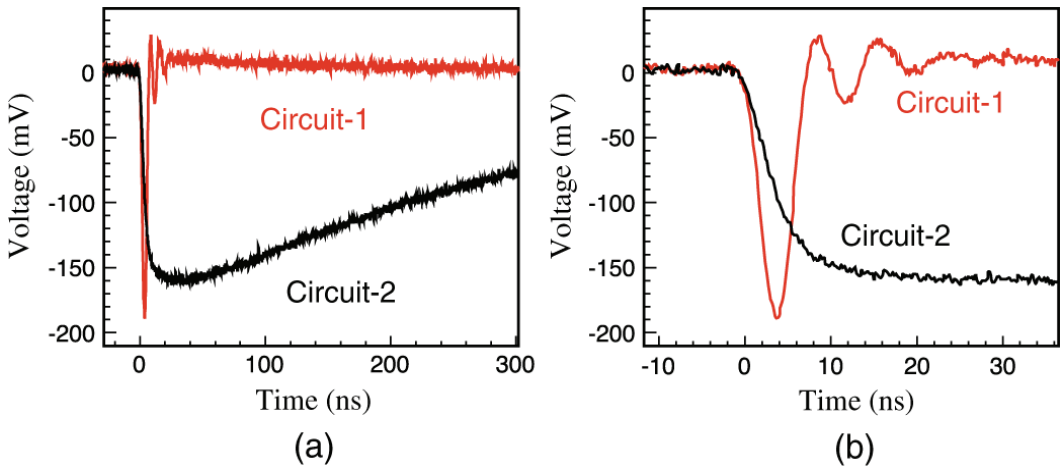

FIG. 24: Pulse shape comparison of the ELPH MPPC readout [30]. (Red) With high pass filter. (Black) Without high pass filter. The right panel shows a zoom of the left panel.

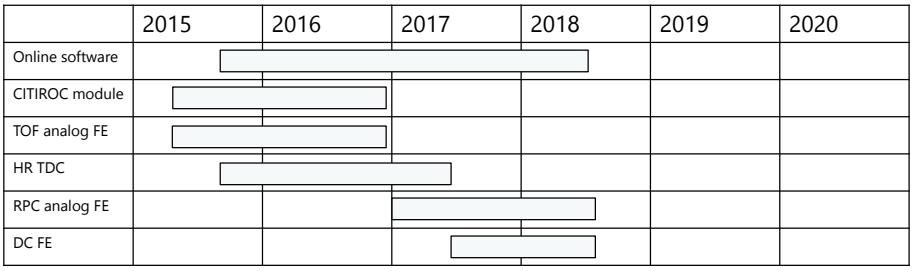

FIG. 25: Schedule of DAQ R&D. A budget for Online software, RPC electronics and DC electronics is not secured at the moment.

G. Wire chamber readout

The ASD chip DC-FEAT [35] (usually called as Belle-II CDC ASD ASIC) has been chosen for wire chamber front-end electronics. For signal digitization, a TDC module with 1 nsec LSB is enough. All-in-one digitizer modules (RECBE [36], [37], RAINER [38]) exist but they are not offered at an affordable price. In order to reduce the production cost, a new module will be developed, where replacing an FPGA and omitting ADCs for waveform sampling are planned for example.

H. Schedule and cost estimation

Figure 25 shows a R&D schedule of E50 DAQ. In 2015, the activity will concentrate on a study of MPPC readout electronics.

The electronics cost is very roughly estimated as 30,000 ch$\times$ 5,000 Yen/ch = 150M Yen.

[1] S. H. Kim, A. Hosaka, H. C. Kim, and H. Noumi, to be published.
[2] S. H. Kim, A. Hosaka, H. C. Kim, H. Noumi, K. Shirotori, Prog. Theor. Exp. Phys. 103D01 (2014).
[3] Hadron Spectrum Collaboration, arXiv:1502.01845; Phys. Rev. **D90**, 074504(2014); Phys. Rev. **D87**, 054506(2013); Phys. Rev. **D85**, 054016(2012); Phys. Rev. **D84**, 074508(2011).
[4] H. Noumi *et al.*, J-PARC Proposal E50, "Charmed Baryon Spectroscopy via the (π, D^{*-}) reaction"(2012).
[5] K. H. Tanaka *et al.*, Nucl. Phys. A **835** (2010) 81.
[6] S. Yokkaichi *et al.*, J-PARC Proposal E16, "Electron pair spectrometer at the J-PARC 50-GeV PS to explore the chiral symmetry in QCD" (2006).
[7] K. Shirotori *et al.*, PoS(Hadron 2013) (2013) 130.
[8] Y. Nara *et al.*, Phys. Rev. C **61** (2000) 024901.
[9] T. Sjöstrand, S. Mrenna and P. Skands, JHEP05 (2006) 026, Comput. Phys. Comm. **178** (2008) 852.
[10] J. H. Christenson *et al.*, Phys. Rev. Lett. **55** (1985) 154.
[11] B. Ghidini *et al.*, Nucl. Phys. B **111** (1976) 189.
[12] R. Honecker *et al.*, Nucl. Phys. B **13** (1969) 571.
[13] F. Barreiro *et al.*, Phys. Rev. D **17** (1978) 669.
[14] D. J. Lange, "The EvtGen particle decay simulation package", Nucl. Instrum. Methods. A **462**, (2001) 152.
[15] T. Yamaga, Master Thesis of Graduate school, Osaka University (2014).
[16] N. Akopov *et al.*, Nucl. Instrum. Methods. A 479 (2002) 511.
[17] A. Sakaguchi *et al.*, J-PARC Proposal E10, "Production of Neutron-Rich Λ-Hypernuclei with the Double Charge-Exchange Reaction" (2006).
[18] R. Honda, Doctral Thesis of Graduate school, Tohoku University (2014).
[19] R. Honecker *et al.*, Nucl. Phys. B **13** (1969) 571.
[20] N. Tomida, Master Thesis of Graduate school, Kyoto University (2012).
[21] I. Kisel, J. Phys. Conf. Ser. **523** (2014) 012022.
[22] M. Nakao *et al.*, IEEE NS **60** (2013) 3729.
[23] Omega/IN2P3, http://omega.in2p3.fr/
WeeROC, http://www.weeroc.com/
[24] J. Fleury *et al.*, JINST **9** (2014) C01049.
[25] EASIROC data sheet.
[26] CITIROC data sheet.
[27] PETIROC2 data sheet.
[28] C. D. Taille, presentation slide of KEK-DTP seminar, April 21, 2015.

[29] P. W. Cattaneo *et al.*, IEEE TNS **61** (2014) 2657.
[30] T. Nishizawa *et al.*, IEEE TNS **61** (2014) 1278.
[31] M. Mota *et al.*, IEEE NSS Conf. Rec. **2** (2000) 9/155
[32] J. Christiansen, HPTDC manual ver. 2.2 for HPTDC chip version 1.3 (2004) http://tdc.web.cern.ch/tdc/hptdc/hptdc.htm
[33] C. Uğur *et al.*, IEEE NoMe TDC, **2013** (2013) 1.
[34] A. Neiser *et al.*, JINST **8** (2013) C12043.
[35] S. Shimazaki *et al.*, NIM A**735** (2014) 193.
[36] T. Uchida *et al.*, IEEE NSS/MIC Conf. Rec. (2011) 694.
[37] N. Taniguchi *et al.*, NIM A**732** (2013) 540.
[38] REPIC, 64ch RAINER MODEL RPR-010, https://www.repic.co.jp/product/module/general/rpr-010.html